NIR-responsive nano-holed titanium alloy surfaces: a photothermally activated antimicrobial biointerface

Denise B. Pistonesi [a, §], Federico Belén [a, §], Juan M. Ruso [b], M. Eugenia Centurión [a], M. Gabriela Sica [c, d], Marcelo F. Pistonesi [a], and Paula V. Messina [a]*

[a] Department of Chemistry, Universidad Nacional del Sur, INQUISUR – CONICET, B8000CPB, Bahía Blanca, Argentina. [b] Soft Matter and Molecular Biophysics Group, Department of Applied Physics, University of Santiago de Compostela, 15782, Santiago de Compostela, Spain. [c] Department of Biology, Biochemistry and Pharmacy, Universidad Nacional del Sur, B8000CPB, Bahía Blanca, Argentina. [d] Department of Health Sciences, Universidad Nacional del Sur, B8000CPB, Bahía Blanca, Argentina.

(*) Author to whom correspondence should be addressed. Tel: +54 291 4595159. Fax: +54 291 4595160. Electronic mail: pmessina@uns.edu.ar.

(§) Denise B. Pistonesi and Federico Belén contributed equally to this work.

Abstract

Among external stimuli - responsive therapy approaches, those using near infrared (NIR) light irradiation have attracted significant attention to treat bone-related diseases and bone tissue regeneration. Therefore, the development of metallic biomaterials sensitive to NIR stimuli is an important area of research in orthopaedics. In this study, we have generated *in situ* prism-shaped silver nanoparticles (*p*-AgNPs) in a biomorphic nano-holed TiO_2 coating on a Ti6Al4V alloy (*a*-Ti6Al4V). Insertion of *p*-AgNPs do not disturb the periodically arranged sub-wavelength-sized unit cell on the *a*-Ti6Al4V dielectric structure, while they exacerbate its peculiar optical response, which results in a higher NIR reflectivity and high efficiency of NIR photothermal energy conversion. Surface dopant reduces the semiconductor optical band gap, spawns a superior density of states in the conduction band and modulates defect sites (e^-/h^+ pairs). Photogenerated e^-/h^+ pairs respond to external NIR light irradiation to attain an optimal antibacterial efficiency. Together, these results open a promising path toward strategic bone therapeutic procedures, providing novel insights into precision medicine.

Keywords: near-infrared radiation, Ti6Al4V alloy, silver nanoparticles, antibacterial properties; photothermal conversion; optical band gap

Introduction

Near infrared light (NIR, 800 - 1300 nm) is administered in advanced targeted healing approaches. [1-4] High yields have been obtained due to its superior penetration capacity and effective transmittance through biological milieu, as well as its minimal damage toward normal tissues, high spatial / temporal precision and easy-to-remote control properties. Current reports have revealed that NIR light-assisted phototherapies are a potential treatment option for bone pathologies, [5, 6] for example, as precise and less invasive solutions for the fracture healing complications. [7] Furthermore, NIR irradiation was shown to exhibit outstanding antioxidant activity and excellent anti-inflammatory effects, decreasing inflammatory cytokines and reducing catabolic proteases, which could effectively alleviate the clinical symptoms of osteoarthritis. [8] Simultaneously, NIR thermal osteogenesis [9, 10] has been scientifically proved *in vitro* and *in vivo*, as well as its ability to treat implant-associated infections. [11] Therefore, the study of NIR-sensitive materials in bone-related therapies is a very auspicious scientific area where the creation of new materials has been increasingly favoured by the rapid development of nanotechnology. In this line of attack, in a previous work, we have developed an electroforming nano-holed TiO_2 coating on Ti6Al4V alloy. [12] This particular metallic−dielectric structure exposed periodically arranged sub-wavelength-sized pores that exhibits higher NIR reflectivity. Following, we have created {111} - faceted silver nanoplates that exhibit a NIR localized surface plasmon resonance (LSPR) extinction spectra. [13] In the present investigation, we have merged both assemblies to generate, in one design, specific light absorption and conversion capabilities in the NIR light window. [14] Titanium and its alloys are currently the most used materials in orthopaedics due to their excellent biocompatibility and mechanical properties. [15] On the other hand, the photocatalytic properties of titanium dioxide [16] make it suitable for photodynamic and photothermal therapies. Here we have

demonstrated that the use of *p*-AgNPs as a "plasmonic sensitizer" enables photothermal conversion by NIR activation of our nano-holed TiO_2 coating and can be exploited against microorganism. Our goal was to construct a versatile NIR light-sensitive metallic platform that potentially satisfies demands of personalized orthopaedics implants.

Experimental Section

Materials

For the synthesis of Ag-NPs in aqueous solution, trisodium citrate ($C_6H_5Na_3O_7 \bullet 2H_2O$, CAS N° 6132-04-3, Biopack); anhydrous glucose (D (+)) ($C_6H_{12}O_6$, CAS N° 50-99-7, Cicarelli); silver nitrate ($AgNO_3$, CAS N° 7761-88-8, Biopack) and L-ascorbic acid ($C_6H_8O_6$, CAS N° 50-81-7, Biopack) were used without further purification. For the preparation of nano-holed TiO_2 coatings, Ti6Al4V sheets (1000 μm thick; Ti 89. 754 %; Al 6.01 %; V 4.06 %; C 0.01 %; N < 0.01 %; O 0.08 %; Fe 0.04 %; H 0.006 %, Others < 0.04 %) were purchased from Roberto Cordes S.A., Buenos Aires, Argentina. Hydrofluoric acid (HF, CAS N° 7664-39-3, 48 wt. %, Sigma -Aldrich), *ortho*-phosphoric acid (H_3PO_4, CAS N° 7664-38-2, 85 wt. % water solution, EMSURE®, Merck), acetone (AC, CAS N° 67-64-1, 99 %, Sigma – Aldrich) and ethanol (EtOH, Art. No. 9065.1, 96%, Carl Roth) have been used as received. All reagents used here were of analytical grade and all solutions were prepared with ultrapure water, 0.05 μS cm^{-1} of electrical conductivity - 18.2 M Ω cm^{-1} of resistivity at 25 ºC, obtained via a Water Purification Systems Millipore - Milli Q, model Elix Technology Inside 10, Merck, France.

Fixation of Silver Nanoplates on Nano - Holed Titanium Alloys Surfaces

Ti6Al4V disks of 10 mm diameter were machined and successively ground with P180, P240, P400, P600, P800, P1000, P1500, P2000 grade SiC abrasive paper and mechanically polished using 3 μm diamond paste (8,000 Grit, Leader Products). Finally, samples were degreased by sonication in AC, EtOH and MQ water for 20 min, in sequence, and dried in an N_2 stream. Anodic TiO_2 coatings (*a*-Ti6Al4V) were electrochemically obtained accordingly to Belen et al. [12] Fixation of silver nanoplates on nano - holed titanium alloys (*a*-Ti6Al4V / *p*-AgNPs) surfaces was performed on basis of two different protocols. (i) Electrochemically anodized TiO_2 coated plates were placed in a container where prism-shaped silver nanoplates (*p*-AgNPs) were synthesized following a previous optimized procedure [13] and left them in the dark for 3, 7 and 11 hours. (ii) On the other hand, 10 mL of *p*-AgNPs were prepared (14 μg mL^{-1}) and concentrated (80 μg mL^{-1}) in a centrifugal - evaporator system (Thermo Scientific Speed Vac SPD11V) at a 35 °C. Then, *a*-Ti6Al4V sheets were submerged in 2 mL of *p*-AgNPs (14 - 80 μg mL^{-1}) during 3, 7 and 11 hours in darkness.

Microstructural and Morphological Characterization

Particle size and morphologies were established by transmission electron microscopy (TEM) using a JEOL 100CX II transmission electron microscope (Jeol Ltd, Tokyo, Japan) operating at 120 kV. A standard procedure of sample preparation was used, in which a droplet of diluted Ag-NPs suspension was deposited and dried at RT on a 200 mesh copper grid covered with a thin layer of transparent carbon film under dust protection. For *a*-Ti6Al4V and *a*-Ti6Al4V / *p*-AgNPs surfaces characterization, a high resolution field emission scanning electron microscopy (HR-SEM) ZEISS ULTRA PLUS, coupled to an

X-ray energy-dispersive (EDX) spectrophotometer that enables elemental chemical microanalysis, was used. Images were acquired with a secondary electron detector (SE2; In lens) operated at an accelerating voltage (EHT) of 3.00 kV and at a working distance (WD) resolution of 2.1 nm. Local compensation of charge was achieved by injecting nitrogen gas. Mean nano-holes diameters, aspect ratio, wall thickness, inter-holes distances, Feret´s diameter (D_F), Feret´s angle (F_{ang}), roundness (R), circularity (C) and 3D surface plots were acquired by digitalized image processing using the free software ImageJ. [17] All statistical values have been obtained using at least 100 measures.

Optical Measurements

Diffusive reflectance patterns were carried out using a Thermo Scientific Spectrophotometer, Nicolet® IS50 FT-IR model provided with near infrared reflectors (CaF_2 / KBr) and detectors (InGaAs / KBr-DLaTGS). Measurements were performed in reflectance mode with a spectral range between 16.000 and 4.000 cm^{-1} (625 – 2500 nm). Spectrums were recorded at 90°of incident radiation on the disks and using the integrated software, at 4 cm^{-1} spectral resolution and by integrating 32 scans. All measurements were carried out at room temperature (RT) employing a custom-made poly-lactic acid (PLA 3D printing filament) sample holder for each angle of incidence radiation, printed on Adonis 3D printer, Hellbot model, and using a Teflon disk as the blank. Molecular fluorescence spectroscopy analysis was performed using a Shimadzu RF-6000 Spectrofluorimeter, in 3D fluorescence mode with a spectral range between 200 and 900 nm for the excitation and emission wavelengths. The spectra were recorded using the integrated software, at 5 nm of spectral resolution and a scanning speed of 12000 nm min^{-1}. For the measurements, home-

made cells printed in PLA were used, which allowed the disks to be placed at angles of 30, 45 and 60° regarding incident radiation, reflecting it towards the detector. Solid absorbance UV –vis measurements were carried out at RT with a UV-Visible Spectrophotometer Evolution 220, Thermo Scientific provided with an integrating sphere accessory. Spectrums were recorded in absorbance mode with a spectral range between 220 nm - 1100 nm; data were acquired with a scan rate of 1200 nm min^{-1} after calibration with Spectralon Diffuse Reflectance standard.

Infrared images of *a*-Ti6Al4V and *a*-Ti6Al4V / *p*-AgNPs surfaces were acquired with a Canon digital camera, Powershot ELPH 190IS model; before capturing images, the camera infrared filter was removed. A tailored system was assembled, which allowed the disks to be located in a closed place, removing the disturbance of external light accordingly to Belen et al. [12] Disks were illuminated using an emitting infrared LED, IR383, λ = 940 nm, controlling the spectral radiant flux, [18] Φ_λ = (1.01 – 38.14) x 10^{-3} mW nm^{-1}, by the application of a Uni-T dimmable source, model UTP3313TFL at RT. Images were compared in terms of the spectral irradiance, E_λ, that is a measure of the radian flux, emitted at a specific wavelength arriving at a point per the differential area surrounding this point; [18] the whole metal disk area, 78.5 mm^2, was considered for the calculus of E_{940}.

Plasmon-based Heat Generation

A physiotherapy NIR 904 nm laser (LB-904, SEAKIT, Buenos Aires, Argentina) which was operated at a 2000 Hz emission frequency (laser radian flux density, irradiance, E = 83.3 mW cm^{-2}), was applied to carry out photothermal experiments. Silver nanoplate

dispersions were placed in glass vials of 11.6 mm diameter and 32 mm height. Laser was adjusted so that the spot can be matched with the area occupied by 700 μL of AgNPs' dispersion, $A \approx 6.3$ cm^{-2}. A similar procedure was performed with *a*-Ti6Al4V and *a*-Ti6Al4V / *p*-AgNPs surfaces. Time evolution thermographs were recorded using a digital thermal imaging camera (CEM High Performance High Resolution Thermal Imagers DT-9873B, CEM Instruments India Pvt Ltd).

Static Contact Angle Measurements

Static contact angle between the disks' surface and a water drop were measured by using a tailored system at RT. [12] The used configuration include a custom-made 3D-sample holder in which the disks were placed at the same height that the digital microscope. Furthermore, at top of the sample holder a tube was connected to form the drop. The other end of the tube was connected to a syringe attached to a syringe pump, Thermometric 612 Syringe Pump 2, forming reproducible drops in all measurements. A maximum drop volume of 2.0 μL was deposited over the disk to acquire the image by the digital microscope (Andonstar Digital Microscope) before static contact angle analyses. All images were processed using the ImageJ software [17] and the contact angles (CA) measurements were done with an accuracy of ± 1 using the Drop Snake and LB-ADSA available module. [19]

Antibacterial Ability

Bacterial Inhibition Growth Capacity

Qualitative preliminary screening of p-AgNPs dispersions capacity to inhibit microbial growth was evaluated by a disk diffusion method using a modified Kirby–Bauer technique. [20] The method was previously standardized by adjusting the microbial inoculation rate, the volume of the agar medium layer and wells of 5 mm in diameter and 50 μL in capacity were made with a sterile glass tube. For inhibition of growth three tester microorganisms from the American Type Culture Collection (ATCC) were considered: Gram-positive, *Staphylococcus aureus* (ATCC: 25923). Bacteria were isolated and stored at Microbiology Chair, Department of Biology, Biochemistry and Pharmacy of the Universidad Nacional del Sur, Argentina. Before their use, microorganisms were cultured in Mueller-Hinton broth (Britania Laboratories, Argentine, B0216906) at 37 °C and allowed to mature overnight to ensure an exponential growth. We have selected *Staphylococcus aureus* as microbial model on basis of it less liability to antibiotic therapy compared with Gram-negative bacteria. [21]

After culturing and harvesting, the strain was re-suspended to maintain the initial concentration of 10^8 colony forming unit per milliliter (CFU mL^{-1}) by spectroscopic adjust (λ = 600 nm) of the optical density at 0.15 accordingly to the McFarland scale. The inoculum concentration was also verified by plating in Plate Count Agar (Britania Laboratories, Argentine, B0211206), incubated at 37 °C for 24 h, using the ISO 4833-1 standard plate count method. [22] Following, 50 μL Ag-NPs dispersions were applied to a hole in the centre of a Mueller-Hinton agar (Britania Laboratories, Argentine, B0213706) plate, previously harvested with bacteria. The agar plates were incubated for 24 h at 37 °C and the diameter of inhibition zone, measured using Image J software, [17] was related to the level of antimicrobial activity present in the sample.

Bacteriostatic and Bactericidal Effect

To study the bacteriostatic effect of the as-prepared p-AgNPs, minimal inhibitory concentration (MIC) was established. The standard broth dilution method [23] was used to study the antimicrobial efficacy of Ag-NPs by evaluating the visible growth of microorganisms in standard nutritive broth (Britania Laboratories, Argentine, B0213706). Serial two-fold dilutions of silver nanoparticles in concentrations ranging from 3.1 to 50.0 μg mL^{-1} with adjusted *Staphylococcus aureus* (ATCC 25923) concentrations (10^6 - 10^2 CFU mL^{-1}) were used to determine MIC. The MIC endpoint is the lowest concentration of silver nanoparticles where no visible growth is seen in the tubes; thus, the visual turbidity comparison of the tubes was noted, both before and after incubation, to confirm the MIC value. The inhibitory effect was also visualized by plating 100 μL aliquots of each Ag-NPs dispersions (50, 25, 12.5, 6.3 and 3.1 μg mL^{-1}) with different *Staphylococcus aureus* (ATCC 25923) concentrations (10^2 to 10^6 CFU mL^{-1}) inoculated in blood agar platelets (Columbia Agar, Sigma-Aldrich, CAS N° 27688, supplemented with 5% v v-1sheep blood) which were then incubated at 37 °C for 24 h. Meanwhile, bactericidal properties were evaluated through a minimum bactericidal concentration (MBC) test and were defined as the lowest Ag-NPs concentration that completely prevented colony forming units. The MBC was determined by sub-culturing 100 μL aliquots of each broth dilutions that inhibit growth of *Staphylococcus aureus* (ATCC 25923); i.e., those at or above the MIC in blood agar petri dishes, incubated at 37 °C for 24 h. In all experiments, bacterial growth without the addition of Ag-NPs and, Ag-NPs´ dispersions without inoculated bacteria were taken as positive (C+) and negative (C-) controls respectively.

Bacteria Viability on a-Ti6Al4V / p-AgNPs Substrates

Staphylococcus aureus (ATCC 25923) were seeded on the substrates at a density of 10^7 CFU mL^{-1} (as estimated by the McFarland scale) by diluting the bacterial cultures to an optical density of 0.52 at 562 nm using a spectrophotometer. The bacteria were allowed to adhere at 37°C throughout 24 hours and at the end of the prescribed time period, the supernatant is removed and the discs are washed 3 times with PBS to eliminate non-adhered bacteria. Finally, 1 mL of PBS was added to a-Ti6Al4V / p-AgNPs substrates, sonicated for 2 min followed by vortexing for 1 min, to loosen the adhered bacteria. To count them, 50 µL of each post-sonication supernatant was collected and counted as previously described in the previous section. The same procedure was applied after irradiating *a*-Ti6Al4V / *p*-AgNPs substrates at 904 nm throughout 10 min; E = 83.3 mW cm^{-2}.

Statistical Analysis

All quantitative assessments were taken at least in triplicate, and results are expressed as mean ± standard deviation (SD). Statistical analysis of data was realized by one factor analysis of variance (ANOVA). Student's t-test and probability values below 0.05 ($p < 0.05$) were considered as a significant difference.

Results and Discussion

Optoelectronic Properties of *a*-Ti6Al4V /*p*-AgNPs Surfaces

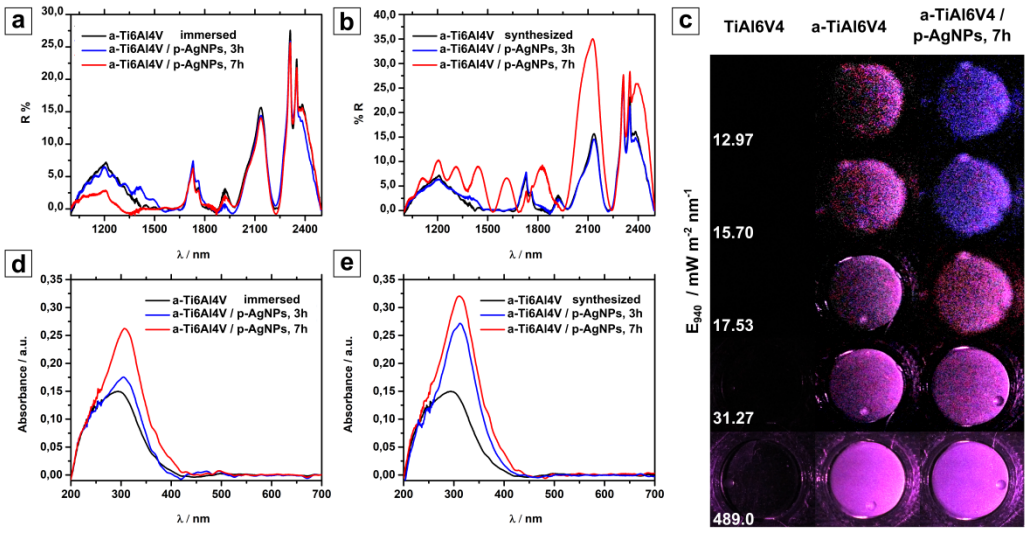

Figure 1. NIR diffuse reflectance of *a*-Ti6Al4V after immersion in: **(a)** *ex-situ* preformed *p*-AgNPs dispersions and **(b)** *in situ* *p*-AgNPs reaction media; measurements were registered after an incident radiation at 90° and RT. **(c)** Optical microphotographs of *a*-Ti6Al4V / p-AgNPs (synthesized, 7h) after NIR irradiation, λ = 940 nm, as a function of spectral irradiance, Eλ; Ti6Al4V and *a*-Ti6Al4V were used as a controls. Absorbance of *a*-Ti6Al4V after immersion in: **(d)** *ex-situ* preformed p-AgNPs dispersions or **(e)** *in situ* *p*-AgNPs reaction media.

Optimizing the photophysical properties of a material is crucial to generating designs with electro-optical functionality. In this sense, we have tested two strategies for incorporating prism-shaped silver nanoplates (*p*-AgNPs) [13] into the anodized titanium surfaces (*a*-Ti6Al4V) [12]: (i) *in situ* generation and (ii) *ex situ* deposition of preformed nanoparticles after immersion of *a*-Ti6Al4V discs in *p*-AgNPs reaction media or in *p*-AgNPs dispersions respectively throughout 3, 7 and 11 hours. Considering that NIR reflectivity is the key point of the peculiar electro-optical response of our previously developed nano-holed titanium alloy surfaces, the effectiveness of the synthesis strategies was evaluated by analyzing the NIR diffuse spectral reflectance of *a*-Ti6Al4V/ *p*-AgNP samples; results are shown in **figures 1a** and **1b**. A broad reflection signal centered at 1200 nm was observed along with

several higher intensity peaks in the mid-infrared regions (1720, 2137 and 2316 nm) that were associated to the effect of radiation on the TiO_2 nano - holed array. [12] No significant statistical differences were observed after immersion of the *a*-Ti6Al4V plates in the dispersion of preformed *p*-AgNPs, **figure 1a**. Conversely, after 7 h of immersion in *p*-AgNPs reaction media, exacerbations of near- and middle - infrared (MIR) wavelengths signals are appreciated, **figure 7b**; no differences are seen by increasing the exposure time to 11 h of treatment. Diffuse reflectance is a useful tool to analyze plasmon structures, as was demonstrated by Victor Ovchinnikov [24]. The author reported that the wavelength position of the LSPR extinction spectra correlates with those of diffuse reflectance in a clear way. Considering that the prism - shaped silver nanoplates have an LSRP extinction spectrum in the range of 400 – 1300 nm, [13] the increase in the intensity of the NIR and MIR signals observed in **figure 1b** could be attributed to the coherent oscillation of the conduction electrons of silver nanoplates *in situ* generated on the electroforming nanostructured substrate. In this way, the radiation emitted by the *p*-AgNPs should be reflected by the titanium substrate within nano-holes, increasing the intensity of the reflection bands. **Figure 1c** shows the reflective results of the *a*-Ti6Al4V and *a*-Ti6Al4V / *p*-AgNPs surfaces after application of a $\lambda = 940$ nm radiation source and regulation of the spectral radiance; bare Ti6Al4V discs are used as control. As expected, both *a*-Ti6Al4V and *a*-Ti6Al4V / *p*-AgNPs surfaces show a shiny appearance compared to polish non-reflective Ti6Al4V substrate, [12] furthermore, a superior effect at low spectral radiance values, $E\lambda \leq 1.96$ W m^{-2} nm^{-1}, of *a*-Ti6Al4V / *p*-AgNPs surfaces is observed. Hybrid samples display a uniform distribution and improve reflectivity along the entire surface, while for *a*-Ti6Al4V the reflection properties are lost as progressing away from the light

source. To corroborate the effect of anisotropic *p*-AgNPs, anodized Ti6Al4V discs immersed in sphere-like AgNPs reaction medium throughout 7h was used as a second control; less reflectivity was observed compared to the original *a*-Ti6Al4V surface; **figure 1SM**.

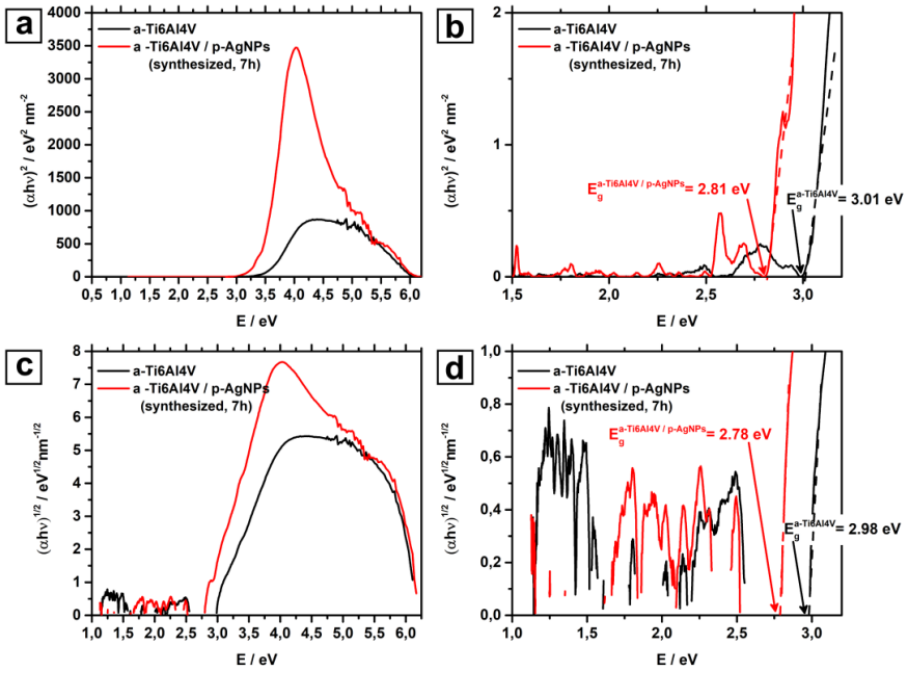

Figure 2. Absorption coefficient, α, was used to analyze the absorption edge for direct **(a, b)** and indirect **(c, d)** transitions respectively.

Olivieri *et al.* [25] reported a plasmonic surface that produces electrically controlled reflectance, in which high sensitivity is achieved from confined surface plasmon. Plasmon absorptions can lead to the creation of a hot electron with sufficient energy to overcome the Schottky barrier at the metal/semiconductor interface. [26] Herein, by combining the localized surface plasmon resonance (LSPR) in the optically NIR excited silver nanoplates; valence electrons of TiO_2 overcome the energy barrier or cross it to become conduction electrons revealed a reflection increment under such conditions. According, we have

analyzed the spectral absorption behavior of tested materials. **Figures 1d** and **1e**, display a strong absorption below a wavelength of about 300 nm in *a*-Ti6Al4V that is associated with the optical band gap of TiO_2. [27] Red shifts and signals intensification are perceived after the exposure of the *a*-Ti6Al4V surface to silver nanoplates. Maximum intensity is observed after immersing the *a*-Ti6Al4V disc in the *p*-AgNPs reaction throughout 7 hours in total agreement with diffuse reflection results, **figure 1b**. The optical band gap energy, E_g, of direct (m = 2) and indirect (m = ½) transitions were estimated from the sharply increasing absorption region according to Tauc and Menth's law [28] by extrapolating the adsorption coefficient (α) to zero in the $(\alpha h\nu)^m$ *vs.* the photon energy (hν) plots. [27, 29] Values of adsorption coefficient (α) were computed using the Kubelka – Munk formalism, [29-31] $\alpha = (1 - R_\infty)^2 / 2R_\infty$, where $R_\infty = R_{sample} / R_{reference}$ is the reflectance of an infinitely thick sample with respect to a reference ($BaSO_4$) at each wavelength; results are shown in **figure 2**. Obtained E_g values of direct transitions, about 3.01 – 2.81 eV, and of indirect transitions, 2.98 – 2.78 eV, agree with those values reported in literature for amorphous TiO_2 [32, 33], while computed E_g for prism-shaped AgNPs dispersions is about 0.98 eV; **figure 2SM**. Narrowing of E_g for *a*-Ti6Al4V / *p*-AgNPs composites agrees with a charge transfer of type-*d* electron of Ag to the conduction band of TiO_2. [34] In addition and according to literature experimental evidence, smaller gaps have been measured for successively disordered systems, as amorphous TiO_2, which explain the presence of lower energy states in **figures 2b** and **2e**. All together with E_g red shift and as a result of the presence of *p*-AgNPs, an important intensification of the absorption coefficient is observed in the energy regime between 3.5 and 4.5 eV. This fact is more evident for direct transitions and can be ascribed to a superior density of states in the conduction band. [29]

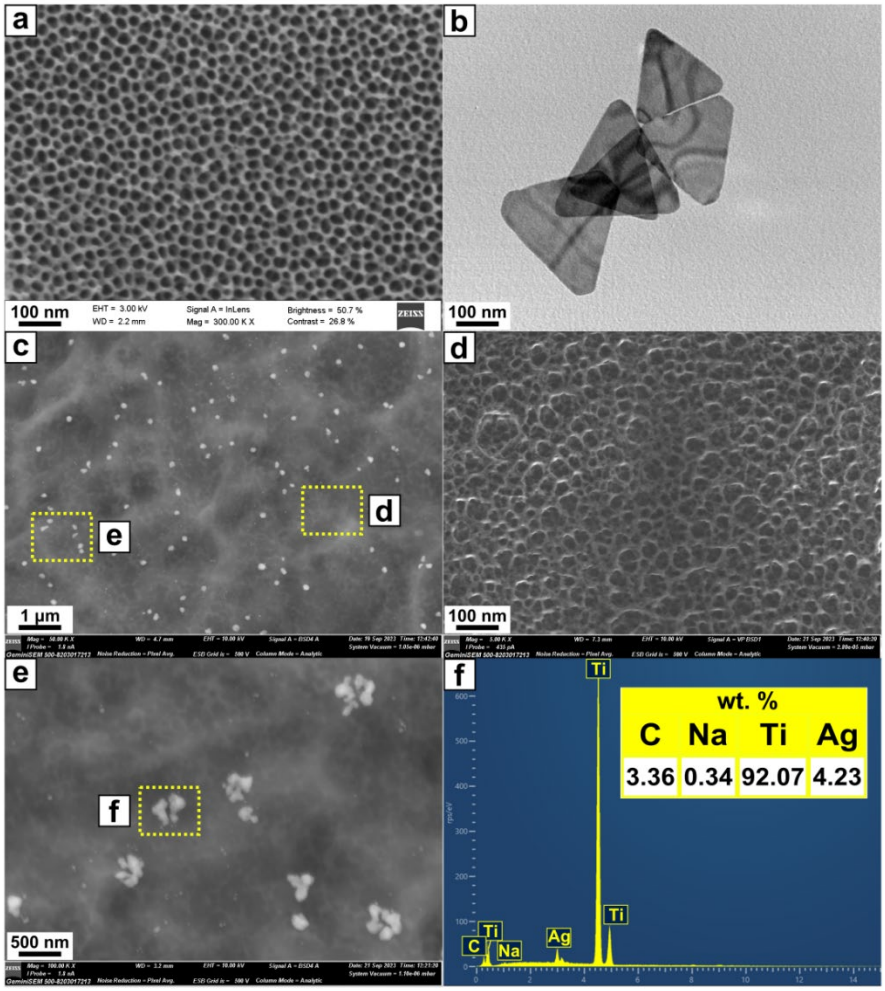

Figure 3 (a) HR-SEM microphotograph of the anodized TiO_2 surface (a-TiAl6V4). [12] **(b)** TEM microphotograph of silver prism - shaped nanoplates (p-AgNPs). [13] **(c)** HR-SEM microphotograph of the anodized TiO_2 surface after nanosilver fixation (a-TiAl6V4 / p-AgNPs). Magnification HR-SEM microphotographs of **(d)** a-TiAl6V4 substrate and **(e)** embedded p-AgNPs. (f) EDX analysis of a-TiAl6V4 / p-AgNPs sample.

Increased absorption coefficient values and red-shift towards NIR band obtained from Ag-content TiO_2 structures was previously reported by Mosquera *et al.* [34] The authors explained such phenomena as a combined effect of larger AgNPs clusters formation along with their surface plasmon resonance originated from nanosilver agglomeration. A careful inspection of *a*-Ti6Al4V / *p*-Ag-NPs surfaces after immersion throughout 7 h in prism-

shaped nanosilver reaction media were examined with high resolution scanning electron microscopy (HR-SEM) being able to correlate electro-optical characteristics with their morphological properties, **figure 3**. Electroformed TiO_2 nano-holed surfaces, *a*-TiAl6V4 [12] and anisotropic prism-shaped nanoplates, p-AgNPs [14] were shown in **figures 3a** and **3b**. Hybrid *a*-TiAl6V4 / *p*-AgNPs materials display a slightly modification of the *a*-TiAl6V4 substrate after *p*-AgNPs fixation, **figures 3c – 3f**. Porous structure is preserved with an increase in the size of the holes, **figure 3d**; no statistically significant differences were detected, **figures 3SM** and **4SM**. After analyzing the 3D reconstructions of the surfaces of *a*-TiAl6V4 and *a*-TiAl6V4 / *p*-AgNPs composites, regularity and periodicity in the distribution of the pores and holes was also comparable; **figures 5SM** and **6SM**. Anisotropic silver nanoparticles are homogeneously deposited on the TiO_2 surface, **figures 3c** and **3e**; the presence of p-AgNPs small clusters fixed on substrate was corroborated from EDX measurements, **figure 3f**, agreeing with the band gaps interpretations previously reported by Mosquera *et al.* [34]

Irradiative recombination of photogenerated electrons and holes (e^- / h^+) and the alteration of local density of states (LDoS) due to the interaction among *p*-AgNPs and *a*-Ti6Al4V should modulate fluorescence emissions of the hybrid surface. [35] 3D photoluminescence (PL) spectra, **figure 4**, are used to corroborate the efficiency of charge trapping, displacement and transference. Anodized Ti6Al4V substrate, **figures 4a**, **4b** and **4c**, presents the characteristic high emission band at $\lambda_{EM} \approx 300$ nm associated with its thin TiO_2 layer band edge emission and to the self-trapped excitons localized on TiO_6 octahedral and oxygen vacancies. [36]

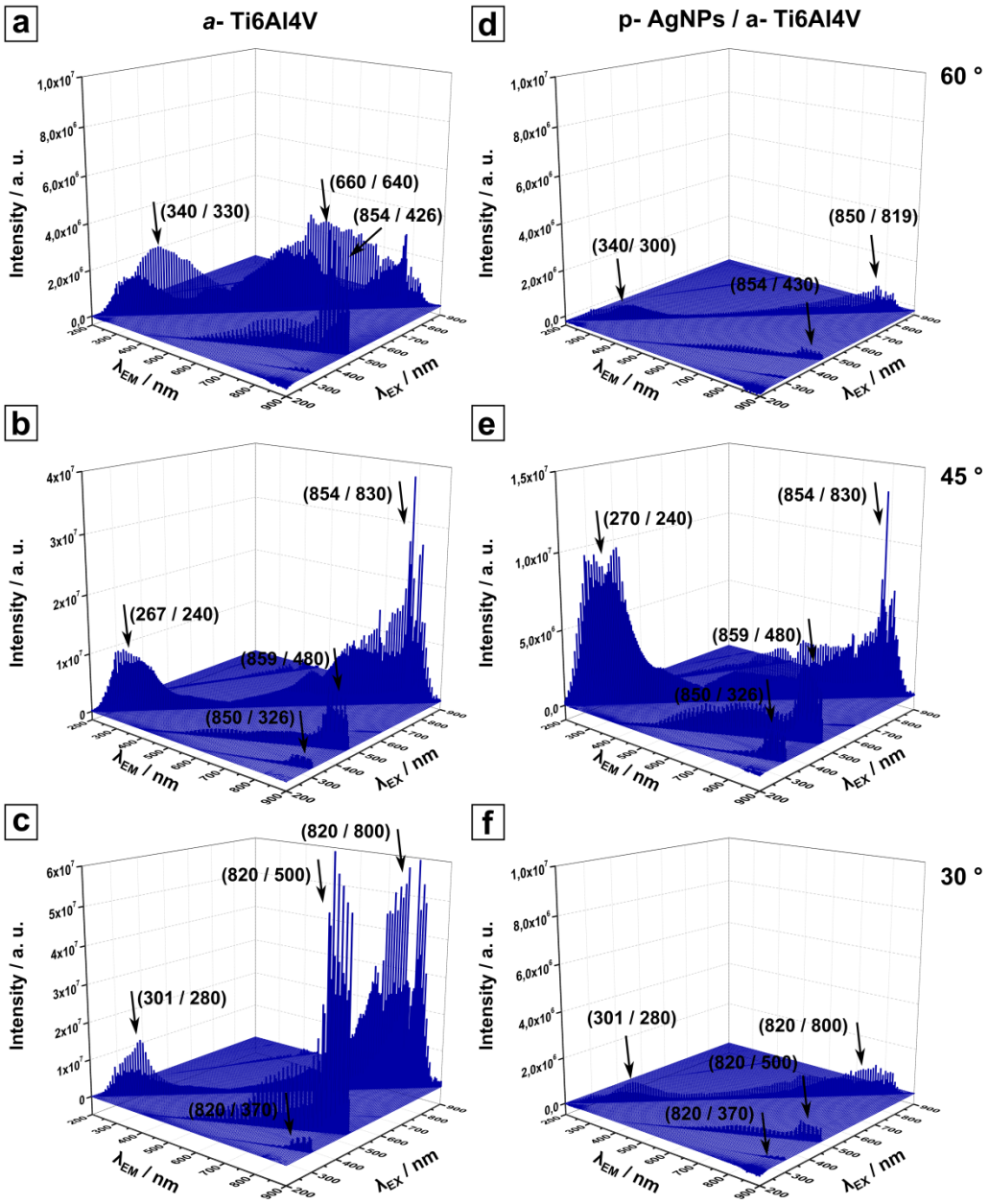

Figure 4. 3D PL patterns recorded at 60, 45 and 30° of incident radiation of the *a*-Ti6Al4V **(a, b, c)** and *a*- Ti6Al4V / *p*-AgNPs **(d, e, f)** surfaces. Peaks indicated with arrows were expressed as (λ_{EM} / λ_{EX}).

Minor peak emissions at larger wavelengths are identified as surface state emissions attributed to the quasi-free recombination at the absorption TiO_2 band edge, the shallow-trap state near the absorption band edge, the deep-trap band far below the band edge, and

permutation of these effects. [36] A hallmarks of the original *a*- Ti6Al4V nanostructure, which acts as a Fabry-Pérot resonator, is the induction of specific oscillations at ≈ 800 nm that respond to the decrease of the incident radiation angle. [12] Nano-holed hierarchical assembly was preserved after the *in situ* generation of nanosilver, **figure 3**, in this way *p*-AgNPs does not alter the Fabry-Pérot resonator behavior. However, prism-like silver nanoparticles effectively suppress PL bands due to the charge separation between TiO_2 and Ag, **figures 4d, 4e** and **4f**. According to literature information, [37, 38] decrease in PL intensity are related to rapid separation sites for photo-generated electrons and holes due to the difference in the energy levels of conduction and valence bands in the two-phase structure of *p*-AgNPs / TiO_2 and to exited electrons that migrate to *p*-AgNPs clusters that prevents the direct recombination. [38] This effect is of lesser intensity when the radiation insides at 45°, in such conditions *p*-AgNPs merely affects the bands associated to de-excitation from lower vibronic levels, in the NIR region (≈ 800 nm), while not to TiO_2 layer band edge emission, **figure 4e**. Further 3D PL patterns are included in the supporting information to demonstrated that the presence of spherical-like AgNPs, which exhibit a surface plasmon in the UV spectral region, [13] exerts a drastic intensity reduction and the disappearance of λ_{EM} ≈ 850 nm vibronic band on the original *a*-Ti6Al4V surface associated with its reflectivity in the NIR which also decreases, **figures 7SM** and **1SM**.

Near-infrared Photothermal Conversion

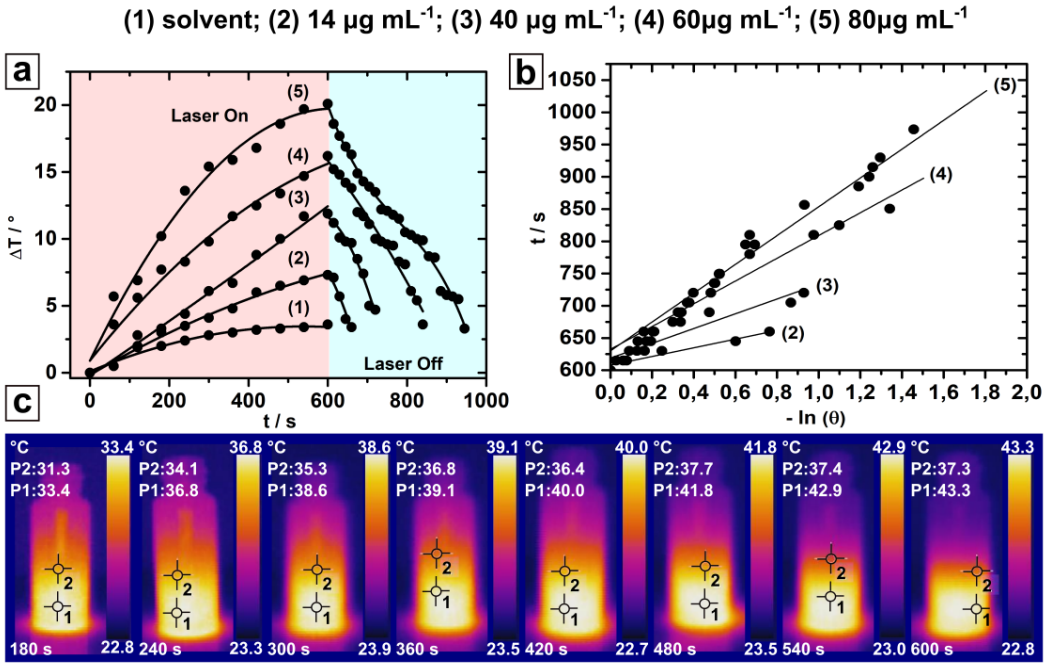

Figure 5. **(a)** Local temperature variation, $\Delta T = T - T_{surr}$, measured at point (1), P1, inside different concentration prism-shaped AgNPs' dispersion during 600 seconds of NIR laser irradiation at 904 nm (E = 83.0 mW cm^{-2}) followed by a cooling period (laser off) until T_{surr}. **(b)** Linearized time data from the cooling period versus negative natural logarithm of driving force temperature (dimensionless parameter, θ) to compute τs. **(c)** Example of IR thermal images of 80 µg mL^{-1} prism-shaped AgNPs' dispersion exposed to a 904 nm (E = 83.6 mW cm^{-2}) laser along 600 seconds; local temperature measured at point (2), r = 6 mm from the central point (P1).

Reductions in the optical band gap of the *p*-AgNPs / *a*-Ti6Al4V surfaces, as well as, higher density of states in the conduction band are consistent with surface dopant behaviour of *p*-AgNPs. In such conditions electrons come from a donor *p*-AgNPs at the *a*-Ti6Al4V surfaces and their activation requires illumination by light [39], as confirmed through the examination of PL patterns, **figure 4**. Following, we analysed photothermal conversion ability to validate the NIR light harvesting capacity. Temperature of tested *p*-AgNP's dispersions increases as the radiation exposure time rises demonstrating the ability of nanoparticles to induce a photothermal (PT) effect, **figures 5a - 5c**. A concentration -

dependent linear behavior was established, providing a rational basis for determination of optimal dosing regimens, **Figure 8SM**. Photothermal conversion efficiency, η, was determined according to a collective heating model based on literature. [40, 41]

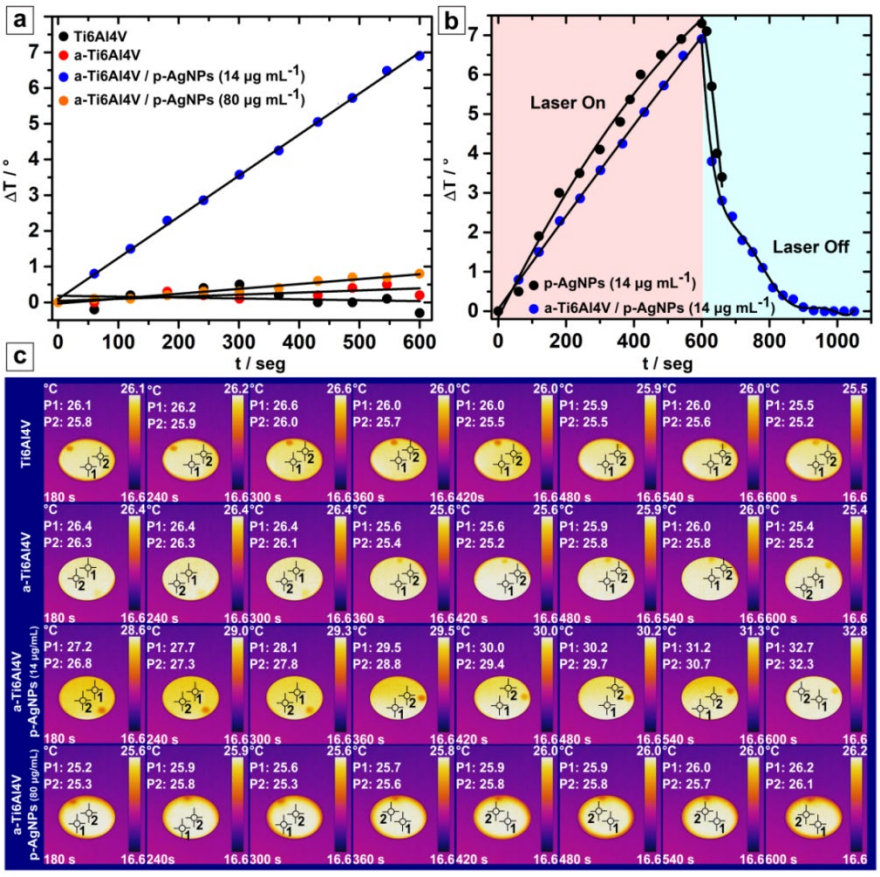

Figure 6. **(a)** Local temperature variation, $\Delta T = T - T_{surr}$, measured at point (1), P1, inside *p*-AgNPs / *a*-Ti6Al4V surfaces during 600 seconds of NIR laser irradiation at 904 nm (E = 83.0 mW cm^{-2}); Ti6Al4V and a-Ti6Al4V discs are used as controls. **(b)** Comparison between local temperature variation, $\Delta T = T - T_{surr}$, measured at point (1), P1, inside 14 μg mL $^{-1}$ concentration prism-shaped AgNPs' dispersion and *p*-AgNPs (14 μg mL $^{-1}$) / *a*-Ti6Al4V surfaces during 600 seconds of NIR laser irradiation at 904 nm (E = 83.0 mW cm^{-2}) followed by a cooling period (laser off) until T_{surr}. **(c)** IR thermal images of Ti6Al4V, a-Ti6Al4V, *in situ* synthesized *p*-AgNPs (14 μg mL $^{-1}$) / *a*-Ti6Al4V and *ex situ* deposited *p*-AgNPs (14 μg mL $^{-1}$) / *a*-Ti6Al4V surfaces exposed to a 904 nm (E = 83.6 mW cm^{-2}) laser along 600 seconds; local temperature measured at point (2), r = 6 mm from the central point (P1).

First, the characteristic time constant for cooling (τ_s) was determined by the introduction of a dimensionless parameter using the maximum system temperature, T_{max}, surroundings temperature, T_{surr}, and by plotting the non-dimensionalized temperature driving force, θ, *vs.* time, t, accordingly to equation (1), following by taking the negative reciprocal of the linear fit data slope, equation (2):

$$\theta = \frac{T - T_{surr}}{T_{max} - T_{surr}} \quad (1)$$

$$t = -\tau_S \ln \theta \quad (2)$$

To determine the heat loss due to external heat flux, Q_{dis}, the linearized form of Newton's Law of Cooling is employed as in equation (3).

$$Q_{dis} = hS(T - T_{surr}) \quad (3)$$

where h is the heat transfer efficiency, S is the surface area of the interface between photothermal material and external environment. External heat flux in the system, Q_{dis}, expresses heat dissipated from the light absorbed by surroundings and was measured independently using a blank that does not contain photothermal material: cuvette and solvent for p-AgNPs dispersions or Ti6Al4V discs as appropriate. To solve the heat-transfer coefficient across the entire area of flux (hS), equation (4) is utilized:

$$\tau_S = \frac{\sum_i m_i C_{p,i}}{hS} \quad (4)$$

where, m_i and $C_{p,i}$ are the mass and heat capacity of the different materials that compose the sample, running through index i. The hS term is then utilized to solve the photothermal conversion efficiency at steady state laser irradiation, where the heat dissipation (Q_{dis}) was subtracted from the overall heat generation according to equation (5).

$$Q_I = hS(T_{max} - T_{surr}) - Q_{dis} \quad (5)$$

Q_I is the energy influx due to photothermal material absorption described as a function of photothermal conversion efficiency, η, by equation (6):

$$Q_I = I\left(1 - 10^{-A^{\lambda}}\right)\eta \quad (6)$$

where I is the laser incident power on each sample computed as $I = E \times A$ and A^{λ} is the absorption of photothermal material at laser irradiation λ.

High values are obtained, η = 49.7 – 65.7 %, which are in the acceptable range for efficient biomedical application, [42] results was summarized in **Table 1SM**. Once the ability of the *p*-AgNPs to induce the PT effect was established, we tested it on *p*-AgNPs / *a*-Ti6Al4V surfaces. It can be appreciated that, in agreement with information exposed in the preceding sections, *p*-AgNPs / *a*-Ti6Al4V surfaces obtained by immersion of *a*-Ti6Al4V discs on *p*-AgNPs reaction media give rise an increase of temperature after NIR laser irradiation while no effect can be seen on bare Ti6Al4V, *a*-Ti6Al4V or in preformed *p*-AgNPs (80 μg mL^{-1}) deposited on *a*-Ti6Al4V discs, **figures 6a -6c**. Truthfully, obtained results are comparable to those obtained with *p*-AgNPs' dispersions of the same concentration with a η = 35 %, **figure 6b** and **table 1SM**.

Antibacterial Properties

The photothermal conversion effect can be used to develop the next generation of controllable antibacterial nano-platforms [43] and, in particular, to control *Staphylococcus Aureus*, examined here, which forms biofilms on bones, heart valves and any implanted medical device.[44] Prism-shaped nanosilver exhibits greater bacteriostatic and bactericidal

effects after direct contact with *Staphylococcus Aureus* that contrast with control spherical-shaped Ag-NPs, **Figure 9SM**. Obtained results are in completely agreement with a shape dependent interaction mechanism related to the presence of higher localized Ag^0 atoms at prims edges. [45] Prism-shaped nanosilver shows a minimum inhibition and bactericidal value of 3.1 μg mL^{-1} at 10^5 CFU mL^{-1} bacterial concentration; results are shown in **figures 6a, 6b** and **Table 2SM**. Once the nanoparticles are blended on the *a*-Ti6Al4V / *p*-AgNPs (14 μg mL^{-1}) substrate, the antibacterial behavior of *p*-AgNPs dispersion is reproduced demonstrating a significant decrease in bacterial colonies density and in their adhesion, **figures 6c** and **6d**. One of the causes of bacterial annihilation is the surface charge of the materials that come into contact with them. It is generally considered that the electrostatic interaction between negatively charged bacteria membrane and positively charged nanoparticles increases the antibacterial efficiency. Electrostatic interaction disturbs the surface negativity of the microorganism membrane by an alteration of lipid mediated signaling and eventually conduces to it destabilization and decease. [46] Accordingly to their isoelectric point 4.4 –5.2, [47, 48] Ti6Al4V, *a*-Ti6Al4V surfaces are negative at pH = 7.4. In addition, *p*-AgNPs zeta potential (ζ-potential) measurements give a value of -33.4 ± 7.4 mV. [13] Being electronegative, *a*-Ti6Al4V / *p*-AgNPs surfaces cause some degree of electrostatic repulsion after interaction with the tested microorganisms (*Staphylococcus aureus* has a ζ-potential values of about −38 mV [49] at 37 °C and physiological pH). Therefore, we did not find any correlation in the reduction of bacterial adhesion with the substrate surface charge. Like the electrostatic interaction, topography and chemical features are additional factors that influence microorganism-surface adhesion and its subsequent viability.

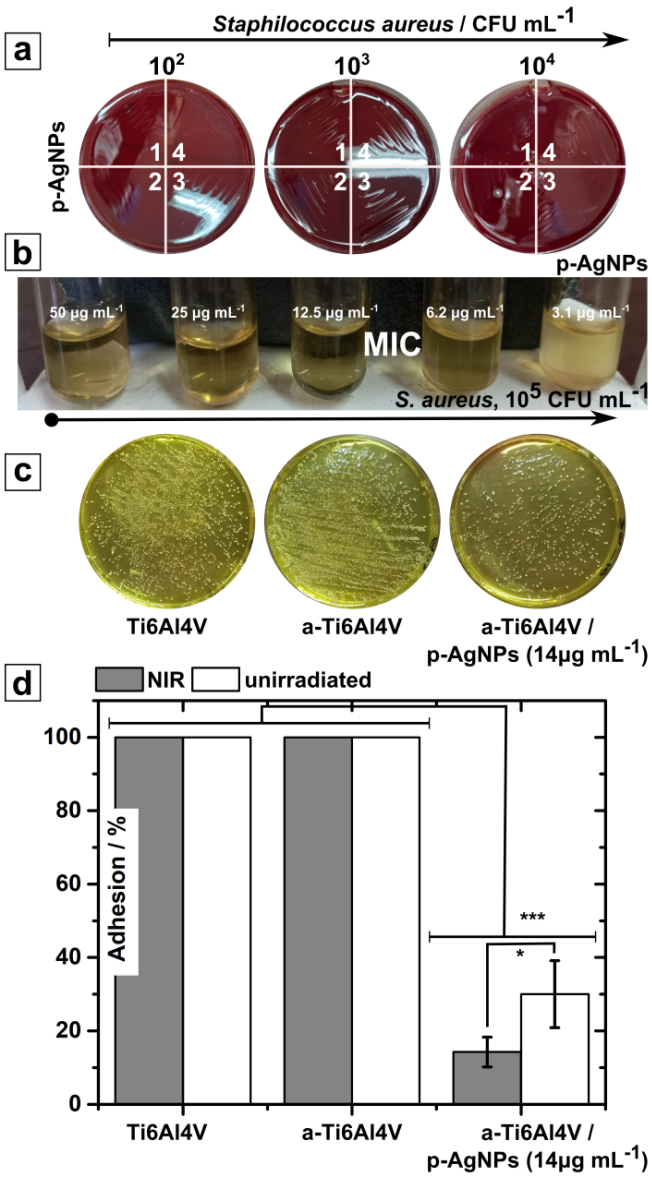

Figure 7. (a) p-AgNPs *Staphylococcus aureus* viability; representative images of *Staphylococcus aureus* with different bacteria concentrations (10^2 - 10^4 CFU mL^{-1}) colonies on blood agar platelets: (1) 25 µg mL^{-1}; (2) 12.5 µg mL^{-1}; (3) 6.2 µg $mL^{-1}$and (4) 3.1 µg mL^{-1}. **(b)** Minimum inhibitory concentration (MIC) endpoint is the lowest concentration of silver nanoparticles where no visible growth is seen in the tubes; thus, the visual turbidity comparison of the tubes was noted, both before and after incubation, to confirm the MIC value. Example of determination of MIC for prism-shaped Ag-NPs against *Staphylococcus aureus* 10^5 CFU mL^{-1} concentration cultured in Mueller Hinton broth at 37 °C for 24 h. **(c)** Bacteria cultures (10^7 CFU mL^{-1}) after interaction with Ti6Al4V, a-Ti6Al4V and p-AgNP/a-Ti6Al4V discs. **(d)** Bacteria adhesion (10^7 CFU mL^{-1}) after 904 nm (E = 83.3 mW cm^{-2}) irradiation of Ti6Al4V, a-Ti6Al4V and p-AgNP/a-Ti6Al4V discs.

In a previous work we have demonstrated that nano-holed coating exhibits a hydrophobic wetting performance according to the Cassie−Baxter regime, even in the presence of chemically hydrophilic compounds. [12] After incorporation of p-AgNPs, wetting features of the surfaces exposed a minor contact angle denoting a higher hydrophilic character compared with original bare Ti6Al4V, **figure 8**.

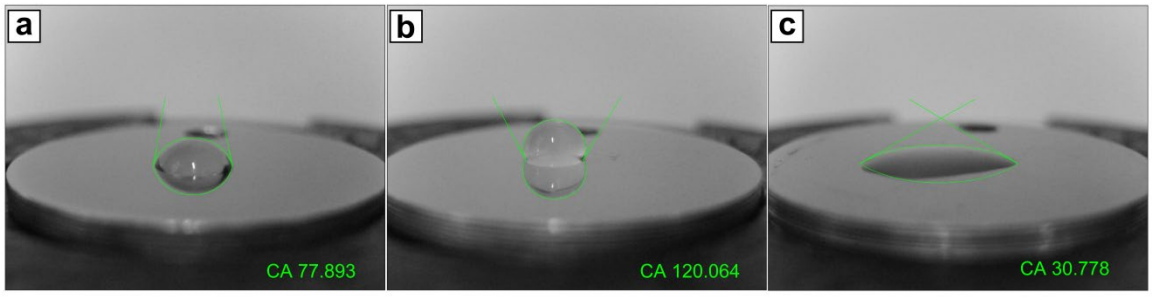

Figure 8. Static water contact angle (CA) measured for **(a)** bare Ti6Al4V, **(b)** *a*-Ti6Al4V, **(c)** *a*-Ti6Al4V / p-AgNP (14 μg mL^{-1}).

It is known that the hydrophilicity of the surfaces favours bacterial adhesion; however in light of the obtained results it is also not possible to correlate the antibacterial effect of *a*-Ti6Al4V / *p*-AgNP (14 μg mL^{-1}) surfaces with their highly hydrophilic character. Similarly, *a*-Ti6Al4V surfaces, despite their strong hydrophobicity, have no antibacterial effect. Once the usual physical and chemical bactericidal effects were ruled out, we tested the effect of heating under NIR irradiation. **Figure 7d** shows that there is a clear reduction of bacterial adhesion and viability after NIR irradiation of *a*-Ti6Al4V / *p*-AgNP (14 μg mL^{-1}) materials compared with bare and anodized Ti6Al4V substrates. We have confirmed that after 10 minutes of NIR irradiation, and despite of a photothermal conversion efficiency of (η) ≈ 50 – 65 %, dispersions of *p*-AgNPs alone do not show any improvement on their

antibacterial capacity, **figure 10SM**. Furthermore, anodized Ti6Al4V sheets, lacking any photothermal effect, shows a 100 % of bacterial adherence with or without irradiation, **figure 7d**. Thus, we have postulate that the photothermal action cannot be isolated from other mechanisms involved in antimicrobial action. Literature information reports that inhibition of colony formation can be performed by manipulation of electronic structure of materials to generate e^-/h^+ vacancies. [50] This mechanism of microorganisms' annihilation fits our previous results, where we have established generation of e^- / h^+ vacancies in the electronic structure of the TiO_2 semiconductor modulated by the incorporation of the *p*-AgNPs, **figures 2** and **4**.

Conclusion

In the present work we have applied the concept of "plasmonic sensitizer", by embedding prism-shaped silver nanoparticles (*p*-AgNPs) assembled within an electroforming nano-holed TiO_2 coating on Ti6Al4V alloy (*a*-Ti6AL4V). In the first part of this work, we have established reaction conditions to attain the maximum photo-conversion capacity under NIR irradiation. We have showed that ordered nano-holed TiO_2 array is a noble substrate for the simple and efficient immobilization of anisotropic plasmonic nanoparticles that present NIR localized surface plasmon resonance (LSPR) extinction spectra. Morphology of nano-holed structure in anodized TiO_2 coating showed no statistical significant differences after *in situ* generation of *p*-AgNPs (14μg mL^{-1}), while their optoelectronic properties are improved. We can demonstrated that radiation emitted due the collective oscillation of the free electrons on the surface of *p*-AgNPs can be reflected by titania substrates within nano-holes, exacerbating near and middle infrared (NIR / MIR) reflection

signals and enhancing surface reflective capacity. Analysis of semiconductor direct and indirect transitions optical band gaps revealed an increased absorption coefficient in agreement with a superior density of states in the conduction band. Recombination of photogenerated electrons and holes, interpreted in terms of 3D photoluminescence (PL) emission patterns, validated the exchange of conduction and valence bands in the *a*-TiAl4V / *p*-AgNPs structure. In the second part of this work, we have evaluated the effectiveness of the electro-optical properties, consequence of *p*-AgNPs insertion on *a*-Ti6Al4V surfaces, in their NIR light harvesting and antibacterial capacity. Hybrid *a*-Ti6Al4V / *p*-AgNPs (14μg mL^{-1}) surfaces exhibited a photothermal conversion efficiency of about 35 % that generated a temperature increment comparable than *p*-AgNPs aqueous dispersion of equivalent concentration. Furthermore antibacterial properties of *a*-Ti6Al4V / *p*-AgNPs (14μg mL^{-1}) surfaces under NIR irradiation are highly superior to those of *a*-Ti6Al4V surface or 14μg mL^{-1}*p*-AgNPs aqueous dispersion separately. The results indicate that there is a synergy of interaction between *a*-Ti6Al4V and *p*-AgNPs and that photothermal effect acts together with other processes involved. A putative mechanism where reduction in the band gap added to the generation of different concentrations of vacancies on TiO_2 semiconductor preventing recombination of photogenerated e^- / h^+ pairs adjusts to the attained bacterial reduction viability.

References

1. Long, K., et al., *Near-infrared light-triggered prodrug photolysis by one-step energy transfer.* Nature Communications, 2023. **14**(1): p. 8112.
2. Peng, J., et al., *Low intensity near-infrared light promotes bone regeneration via circadian clock protein cryptochrome 1.* International Journal of Oral Science, 2022. **14**(1): p. 53.
3. Walski, T., et al., *Near-infrared photobiomodulation of blood reversibly inhibits platelet reactivity and reduces hemolysis.* Scientific Reports, 2022. **12**(1): p. 4042.
4. Yu, Y., et al., *Photothermogenetic inhibition of cancer stemness by near-infrared-light-activatable nanocomplexes.* Nature Communications, 2020. **11**(1): p. 4117.
5. Wan, Z., et al., *NIR light-assisted phototherapies for bone-related diseases and bone tissue regeneration: A systematic review.* Theranostics, 2020. **10**(25): p. 11837.
6. Feng, Q., X. Zhou, and C. He, *NIR light-facilitated bone tissue engineering.* Wiley Interdisciplinary Reviews: Nanomedicine and Nanobiotechnology, 2024. **16**(1): p. e1925.
7. Quirk, B.J., et al., *Effect of near-infrared light on in vitro cellular ATP production of osteoblasts and fibroblasts and on fracture healing with intramedullary fixation.* Journal of Clinical Orthopaedics and Trauma, 2016. **7**(4): p. 234-241.
8. Shi, G., et al., *NIR-responsive molybdenum (Mo)-based nanoclusters enhance ROS scavenging for osteoarthritis therapy.* Pharmacological Research, 2023. **192**: p. 106768.
9. Wang, S., et al., *The effect of near-infrared light-assisted photothermal therapy combined with polymer materials on promoting bone regeneration: A systematic review.* Materials & Design, 2022. **217**: p. 110621.
10. Li, C., et al., *NIR-responsive composite nanofibers provide oxygen and mineral elements to promote osteogenesis.* Materials & Design, 2022. **224**: p. 111285.
11. Zhang, G., et al., *Near-infrared light II-assisted rapid biofilm elimination platform for bone implants at mild temperature.* Biomaterials, 2021. **269**: p. 120634.
12. Belén, F., et al., *NIR-Reflective and Hydrophobic Bio-Inspired Nano-Holed Configurations on Titanium Alloy.* ACS Applied Materials & Interfaces, 2022. **14**(4): p. 5843-5855.
13. Pistonesi, D.B., et al., *{111} - Faceted Silver Nanoplates: An Automated and Customized Design for Functionality.* ChemNanoMat, 2023. **n/a**(n/a): p. e202300354.
14. Smith, A.M., M.C. Mancini, and S. Nie, *Bioimaging: second window for in vivo imaging.* Nat Nanotechnol, 2009. **4**(11): p. 710-1.
15. Bandyopadhyay, A., et al., *Improving biocompatibility for next generation of metallic implants.* Progress in Materials Science, 2023. **133**: p. 101053.
16. Wold, A., *Photocatalytic properties of titanium dioxide (TiO2).* Chemistry of Materials, 1993. **5**(3): p. 280-283.
17. Schneider, C.A., W.S. Rasband, and K.W. Eliceiri, *NIH Image to ImageJ: 25 years of image analysis.* Nat. Methods, 2012. **9**(7): p. 671-675.
18. Choudhury, A.K.R., *Characteristics of light sources.* Principles of Colour and Appearance Measurement, 2014: p. 1-52.
19. Stalder, A.F., et al., *A snake-based approach to accurate determination of both contact points and contact angles.* Colloids and surfaces A: physicochemical and engineering aspects, 2006. **286**(1-3): p. 92-103.
20. Hudzicki, J., *Kirby-Bauer disk diffusion susceptibility test protocol.* ASM, 2009. **15**: p. 55-63.
21. Parastan, R., et al., *Staphylococcus aureus biofilms: Structures, antibiotic resistance, inhibition, and vaccines.* Gene Rep., 2020. **20**: p. 100739.

22. ISO, *ISO 4833 2 2013(E). Microbiology of the food chain — Horizontal method for the enumeration of microorganisms — Part 2: Colony count at 30 °C by the surface plating technique*. 2013.
23. Weinstein, M.P. and J.S. Lewis, *The clinical and laboratory standards institute subcommittee on antimicrobial susceptibility testing: background, organization, functions, and processes.* J. Clin. Microbiol., 2020. **58**(3): p. e01864-19.
24. Ovchinnikov, V., *Reflection from disordered silver nanoparticles on multilayer substrate.* Sensors & Transducers, 2015. **193**(10): p. 170.
25. Olivieri, A., et al., *Plasmonic nanostructured metal-oxide-semiconductor reflection modulators.* Nano Lett, 2015. **15**(4): p. 2304-11.
26. Mishra, A.K., et al., *Plasmonic solar energy harvesting by ZnO nanostructures and their composite interfaces: a review on fundamentals, recent advances, and applications.* Energy Technology, 2023. **11**(7): p. 2201393.
27. Ruso, J.M., et al., *Enhancing CaP biomimetic growth on TiO2 cuboids nanoparticles via highly reactive facets.* Langmuir, 2013. **29**(7): p. 2350-2358.
28. Tauc, J. and A. Menth, *States in the gap.* Journal of non-crystalline solids, 1972. **8**: p. 569-585.
29. Reyes-Coronado, D., et al., *Phase-pure TiO2 nanoparticles: anatase, brookite and rutile.* Nanotechnology, 2008. **19**(14): p. 145605.
30. Ciani, A., K.U. Goss, and R.P. Schwarzenbach, *Light penetration in soil and particulate minerals.* European journal of soil science, 2005. **56**(5): p. 561-574.
31. Nishanthi, S., et al., *Plasmonic silver nanoparticles loaded titania nanotube arrays exhibiting enhanced photoelectrochemical and photocatalytic activities.* Journal of Power Sources, 2015. **274**: p. 885-893.
32. Gonçalves, M.C., et al., *Photonic band gap and bactericide performance of amorphous sol-gel titania: An alternative to crystalline TiO2.* Molecules, 2018. **23**(7): p. 1677.
33. Deskins, N.A., J. Du, and P. Rao, *The structural and electronic properties of reduced amorphous titania.* Physical Chemistry Chemical Physics, 2017. **19**(28): p. 18671-18684.
34. Mosquera, A.A., et al., *Effect of silver on the phase transition and wettability of titanium oxide films.* Scientific Reports, 2016. **6**(1): p. 32171.
35. Shokry, A., et al., *Highly Luminescent Ternary Nanocomposite of Polyaniline, Silver Nanoparticles and Graphene Oxide Quantum Dots.* Sci Rep, 2019. **9**(1): p. 019-53584.
36. Mathew, S., et al., *UV-visible photoluminescence of TiO 2 nanoparticles prepared by hydrothermal method.* J. Fluoresc., 2012. **22**(6): p. 1563-1569.
37. Fukuhara, D., et al., *Local Silver Site Temperature Critically Reflected Partial and Complete Photooxidation of Ethanol Using Ag–TiO2 as Revealed by Extended X-ray Absorption Fine Structure Debye–Waller Factor.* The Journal of Physical Chemistry C, 2021. **125**(27): p. 14689-14701.
38. Kumar, D.P., et al., *Solar light sensitized p-Ag2O/n-TiO2 nanotubes heterojunction photocatalysts for enhanced hydrogen production in aqueous-glycerol solution.* Solar Energy Materials and Solar Cells, 2016. **154**: p. 78-87.
39. Zhang, H., et al., *Theory of quantum plasmon resonances in doped semiconductor nanocrystals.* The Journal of Physical Chemistry C, 2014. **118**(29): p. 16035-16042.
40. Jiang, K., D.A. Smith, and A. Pinchuk, *Size-dependent photothermal conversion efficiencies of plasmonically heated gold nanoparticles.* J. Phys. Chem. C, 2013. **117**(51): p. 27073-27080.

41. Liu, X., et al., *Facile synthesis of biocompatible cysteine-coated CuS nanoparticles with high photothermal conversion efficiency for cancer therapy.* Dalton Trans., 2014. **43**(30): p. 11709-11715.
42. Ren, Y., Y. Yan, and H. Qi, *Photothermal conversion and transfer in photothermal therapy: From macroscale to nanoscale.* Advances in Colloid and Interface Science, 2022. **308**: p. 102753.
43. Dediu, V., et al., *Trends in Photothermal Nanostructures for Antimicrobial Applications.* Int J Mol Sci, 2023. **24**(11).
44. Lister, J.L. and A.R. Horswill, *Staphylococcus aureus biofilms: recent developments in biofilm dispersal.* Front Cell Infect Microbiol, 2014. **4**(178).
45. Helmlinger, J., et al., *Silver nanoparticles with different size and shape: equal cytotoxicity, but different antibacterial effects.* RSC Adv., 2016. **6**(22): p. 18490-18501.
46. Placente, D., et al., *Self-fluorescent antibiotic MoO x–hydroxyapatite: a nano-theranostic platform for bone infection therapies.* Nanoscale, 2019. **11**(37): p. 17277-17292.
47. Roessler, S., et al., *Characterization of oxide layers on Ti6Al4V and titanium by streaming potential and streaming current measurements.* Colloids and Surfaces B: Biointerfaces, 2002. **26**(4): p. 387-395.
48. D'Elia, N.L., et al., *Albumin-mediated deposition of bone-like apatite onto nano-sized surfaces: Effect of surface reactivity and interfacial hydration.* J Colloid Interface Sci, 2017. **494**: p. 345-354.
49. Kłodzińska, E., et al., *Effect of zeta potential value on bacterial behavior during electrophoretic separation.* Electrophoresis, 2010. **31**(9): p. 1590-1596.
50. Wu, G., et al., *NIR light responsive MoS2 nanomaterials for rapid sterilization: Optimum photothermal effect via sulfur vacancy modulation.* Chemical Engineering Journal, 2022. **427**: p. 132007.